

Chapter 7

Theoretical Properties of Materials Formed as Wire Network Graphs from Triply Periodic CMC Surfaces, Especially the Gyroid



Ralph M. Kaufmann and Birgit Wehefritz-Kaufmann

Abstract We report on our recent results from a mathematical study of wire network graphs that are complements to triply periodic CMC surfaces and can be synthesized in the lab on the nanoscale. Here, we studied all three cases in which the graphs corresponding to the networks are symmetric and self-dual. These are the cubic, diamond and gyroid surfaces. The gyroid is the most interesting case in its geometry and properties as it exhibits Dirac points (in 3d). It can be seen as a generalization of the honeycomb lattice in 2d that models graphene. Indeed, our theory works in more general cases, such as periodic networks in any dimension and even more abstract settings. After presenting our theoretical results, we aim to invite an experimental study of these Dirac points and a possible quantum Hall effect. The general theory also allows to find local symmetry groups which force degeneracies aka level crossings from a finite graph encoding the elementary cell structure. Vice-versa one could hope to start with graphs and then construct matching materials that will then exhibit the properties dictated by such graphs.

7.1 Introduction

We will first start to review the main motivating examples for our analysis and our methods. These are the triply periodic constant mean curvature (CMC) surfaces which are very intriguing objects due to their highly symmetric nature. By a classification result, the only triply periodic minimal surfaces whose complements are given by symmetric and self-dual graphs are the P (cubic), D (diamond) and G (gyroid)

R. M. Kaufmann

Department of Mathematics, Purdue University, 150 N. University Street,
West Lafayette, IN 47907, USA

e-mail: rkaufman@math.purdue.edu

B. Wehefritz-Kaufmann (✉)

Department of Mathematics and Department of Physics and Astronomy,
Purdue University, 150 N. University Street, West Lafayette, IN 47907, USA

e-mail: ebkaufma@math.purdue.edu

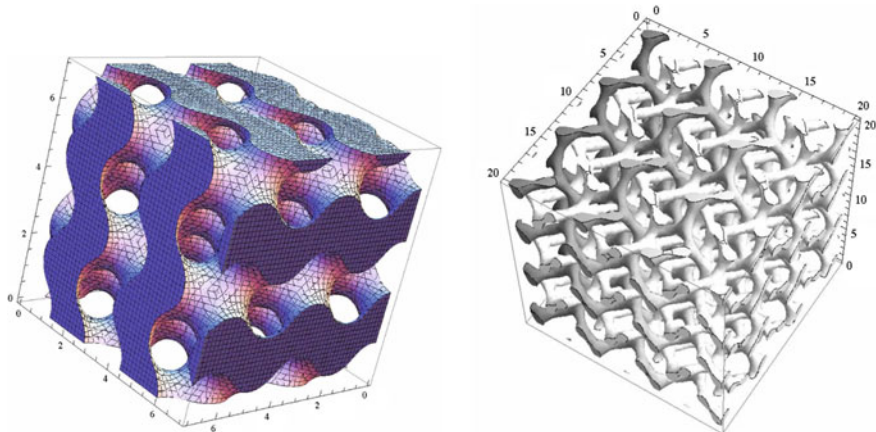


Fig. 7.1 The double gyroid surface (left) and its complement, the two non-intersecting channel systems C_+ and C_- (right)

surfaces (see e.g. [1]). While the cubic and diamond surfaces have been known for almost two centuries (they were already discovered by Schwarz in 1830 [2]), the gyroid was an omission in Schwarz's classification and was only discovered about 50 years ago in 1970 by Alan Schoen [3]. As any naturally occurring surface, a physical version will not be a true 2d object, but will have some, albeit small thickness, which makes it 3d. Such a thick surface has two sides, each a true 2d surface. Thus, the interface actually consists of *two* disconnected surfaces, where *each* of them is a surface of the given type. The double gyroid (DG) for instance is such a configuration of two mutually non-intersecting embedded gyroids which form the boundaries of the thick gyroid surface.

A single gyroid has symmetry group $I4_132$ while the double gyroid has the symmetry group $Ia\bar{3}d$ where the extra symmetry comes from interchanging the two gyroids.¹

The actual equations of the gyroid are very complicated and initially only locally known by a differential equation since it is a CMC surface. To get the true shape mathematically one can use a computer program, the Brakke Surface Evolver [5]. However, in a good approximation, the surfaces can be visualized by using the level surfaces [6]. An example of a level surface approximation for the double gyroid is given by the following formula:

$$L_t : \sin(x) \cos(y) + \sin(y) \cos(z) + \sin(z) \cos(x) = t$$

which we use in the visualizations. The double gyroid surface is then modeled by L_t and L_{-t} for $0 < t < \sqrt{2}$. It is pictured in Fig. 7.1.

¹Here $I4_132$ and $Ia\bar{3}d$ are given in the international or Hermann–Mauguin notation for symmetry groups, see e.g. [4].

Recently, it was demonstrated that the gyroid can be synthesized in the lab [7]. Both the surface and its complement, which forms a two-channel network (see Fig. 7.1), can be realized by using nano-porous silica film. It is interesting to note that the gyroid structure appears spontaneously in nature on the wings of certain butterflies or beetles to give them their brilliant color [8].

Several variations of these structures have been synthesized, i.e. semiconductor quantum-wire arrays of PbSe, PbS, and CdSe. The synthesis process involves several steps. First, the actual surface nanostructure is formed by self-assembly in some carefully prepared surfactant or block copolymer systems. The nanopores (channels) are then filled with a semiconductor and the original silica surface is dissolved to yield the nanowire network. A second semiconductor material may potentially be grown in the void space to yield a bulk heterojunction semiconductor. The typical lattice constant of these structures is of the order of 18 nm. This means that they are “supercrystals”, with lattice constants far exceeding atomic length scales. However, a quantum mechanical treatment is still applicable and the typical length scale is comparable with graphene (where the length scale is of the order of 10 nm). We will focus on the wire structure in this article.

We performed a theoretical study to predict properties of these materials. Our approach is comprised of an analysis of the symmetries, the singularities and a non-commutative model all of which we will briefly explain. This treatment is not restricted to the particular example of the gyroid and can be used to study any periodic wire network and even further generalizations. We have applied it to the cases of the wire networks derived from the cubic, the diamond and the gyroid triply periodic CMC surfaces as well as other periodic structures such as Bravais lattices and the honeycomb lattice underlying graphene.

7.1.1 *Classical Geometry of the Gyroid and Graph Approximation for the Channels*

Let us first describe in more detail the classical geometry of the gyroid. Details can be found in [9]. The complement $\mathbb{R}^3 \setminus G$ of a single gyroid G has two components. These components will be called the gyroid wire systems or channels.

There are two distinct channels, one left and one right handed. Each of these 3d channels can be contracted onto an embedded graph, called skeletal graph [3, 10]. We will call these graphs Γ_+ and Γ_- . Each graph is periodic and trivalent. We fix Γ_+ to be the graph which has the node $v_0 = (\frac{5}{8}, \frac{5}{8}, \frac{5}{8})$ in the above approximation. We will give more details on the graph Γ_+ below.

The channel containing Γ_+ is shown in Fig. 7.2a. A (crystal) unit cell of the channel together with the embedded graph Γ_+ is shown in Fig. 7.2b and just the skeletal graph is contained in Fig. 7.2c. The unit cell is obtained by using the simple lattice translations along the x , y and z axes. Such a cell contains 8 vertices which are trivalent. The actual symmetry group is bcc and hence higher. If one mods out

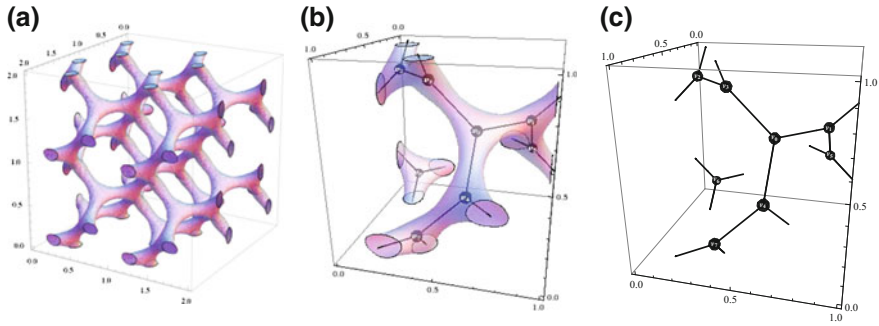
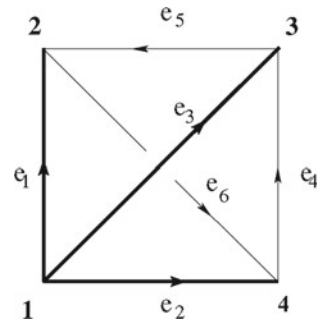


Fig. 7.2 **a** 3d periodic structure of the gyroid wire network **b** skeletal graph inside the channel **c** skeletal graph with labeled vertices

Fig. 7.3 Abstract quotient graph used in our calculation. The bold edges are a spanning tree and the vertex 1 is a root of this spanning tree



by the full symmetry group then an elementary cell will only have 4 points which are trivalent. This is captured by a graph with 4 vertices where each vertex is linked to all other vertices. This graph, which is called the full square or the tetrahedral graph, is abstract. This means that it is not embedded in any real space, but just a combinatorial object, see Fig. 7.3.

Stating things in a more precise fashion: The graph Γ_+ is the graph made up of the following vertices in the unit cell

$$\begin{aligned}
 v_0 &= \left(\frac{5}{8}, \frac{5}{8}, \frac{5}{8}\right) & v_4 &= \left(\frac{7}{8}, \frac{5}{8}, \frac{3}{8}\right) \\
 v_1 &= \left(\frac{3}{8}, \frac{7}{8}, \frac{5}{8}\right) & v_5 &= \left(\frac{1}{8}, \frac{7}{8}, \frac{3}{8}\right) \\
 v_2 &= \left(\frac{3}{8}, \frac{1}{8}, \frac{7}{8}\right) & v_6 &= \left(\frac{1}{8}, \frac{1}{8}, \frac{7}{8}\right) \\
 v_3 &= \left(\frac{5}{8}, \frac{3}{8}, \frac{7}{8}\right) & v_7 &= \left(\frac{7}{8}, \frac{3}{8}, \frac{1}{8}\right),
 \end{aligned} \tag{7.1}$$

and all their translations along the lattice directions and the edges between them according to the incidences that can be read off from Fig. 7.2.

By combinatorial arguments, we have obtained results about the classical geometry of the infinite graph Γ_+ [9]. Namely, there are closed loops on the graph Γ_+ . Each minimal loop goes through 10 sites and at each point there are 30 oriented minimal loops or 15 such undirected loops.

As mentioned, the translational symmetry group for both the gyroid and the double gyroid is actually the body-centered cubic (bcc) lattice. In our theoretical calculations, we will deal with a finite graph that is obtained as a quotient graph from Γ_+ . We can use the bcc symmetry of the lattice to construct this abstract quotient graph. A set of generators of the bcc symmetry is

$$g_1 = \frac{1}{2}(1, -1, 1), \quad g_2 = \frac{1}{2}(-1, 1, 1), \quad g_3 = \frac{1}{2}(1, 1, -1) \quad (7.2)$$

The passage from the graph of the unit cell with 8 vertices is given by identifying the vertices. $v_0 \leftrightarrow v_6$, $v_1 \leftrightarrow v_7$, $v_2 \leftrightarrow v_4$ and $v_3 \leftrightarrow v_5$. The 6 edge vectors are then represented by the 6 vectors

$$e_1 = \frac{1}{4} \begin{pmatrix} -1 \\ 1 \\ 0 \end{pmatrix}, \quad e_2 = \frac{1}{4} \begin{pmatrix} 0 \\ -1 \\ 1 \end{pmatrix}, \quad e_3 = \frac{1}{4} \begin{pmatrix} 1 \\ 0 \\ -1 \end{pmatrix} \quad (7.3)$$

$$e_4 = \frac{1}{4} \begin{pmatrix} 1 \\ 1 \\ 0 \end{pmatrix}, \quad e_5 = \frac{1}{4} \begin{pmatrix} 0 \\ -1 \\ -1 \end{pmatrix}, \quad e_6 = \frac{1}{4} \begin{pmatrix} -1 \\ 0 \\ -1 \end{pmatrix} \quad (7.4)$$

Now, the translates of the points v_i , $i = 1, \dots, 4$ along integer linear combinations of the g_j , $j = 1, 2, 3$ and the translates of the edge vectors e_k , $k = 1, \dots, 6$ form the graph Γ_+ . Taking the quotient by the free Abelian subgroup L that is generated by the vectors g_i , we arrive at the abstract quotient graph $\bar{\Gamma} = \Gamma_+/L$. It is the graph with 4 vertices and 6 edges, where all pairs of distinct vertices are connected by exactly one edge shown in Fig. 7.3. It turns out that this graph basically suffices to capture the essential information about the geometry.

The passage from the channel systems to the graphs retains all homotopical information as does the passage from the thick surface to just one copy of the gyroid, by shrinking the thickness to zero. Any topological information which is homotopy invariant (that is basically the information that is invariant under continuous deformations) is encoded in the gyroid surface and the two skeletal graphs. Furthermore, since the level surface approximation is a deformation of the original gyroid, one can use this simplification for the study. Notice that not all geometric information is retained by such a deformation, for instance being a CMC surface is not. Also, as we have seen, dimensions are not preserved either, what is preserved, however, are topological charges, singularities, homology, K-theory, etc. These deformation independent quantities are of course very desirable as a physically realized version

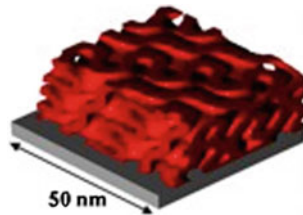


Fig. 7.4 Fabricated gyroid structure squished by gravity [11]

of the gyroid will not be perfect. Indeed the result of the gyroid, the self-assembly is actually a gyroid, that is a bit squished, see Fig. 7.4.

The fact that the skeletal graph approximation is valid for the electronic properties has been shown by a different physical argument: namely, numerical simulations of a simple wave equation [12] have shown that the lowest-energy wavefunctions are supported primarily on the junctions. Thus, one may expect to reproduce the low-energy end of the spectrum by using the tight-binding approximation, in which the junctions are replaced by the vertices, and the segments connecting them by the edges of a graph.

We can and will thus continue the study of the wire system by using the graph approximation.

7.1.2 *P and D Surfaces*

There are two other triply periodic self-dual and symmetric CMC surfaces- the cubic (P) and the diamond (D) network. They are shown in Fig. 7.5 together with their wire networks obtained in the same way as for the gyroid. Here we summarize the results from [13].

The P surface has a complement which has two connected components each of which can be retracted to the simple cubical graph whose vertices are the integer lattice $\mathbb{Z}^3 \subset \mathbb{R}^3$. The translational group is \mathbb{Z}^3 in this embedding, so it reduces to the case of a Bravais lattice. Its abstract quotient graph is shown in Fig. 7.6 on the left.

The D surface has a complement consisting of two channels each of which can be retracted to the diamond lattice Γ_\diamond . The diamond lattice is given by two copies of the fcc lattice, where the second fcc is the shift by $\frac{1}{4}(1, 1, 1)$ of the standard fcc lattice, see Fig. 7.5. The edges are nearest neighbor edges. The symmetry group is $Fd\bar{3}m$. The quotient graph for the D surface is shown in Fig. 7.6 on the right.

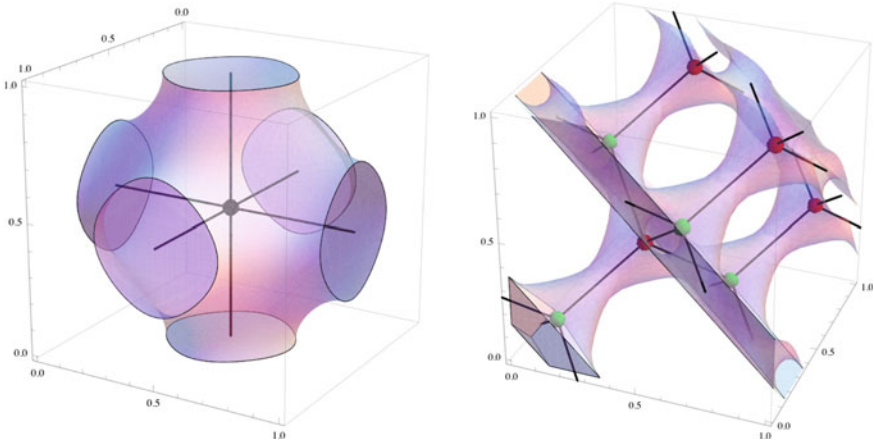
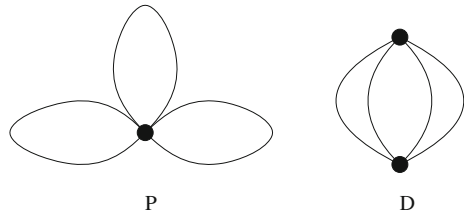


Fig. 7.5 The cubic (P) (left) and the diamond (D) wire network (right)

Fig. 7.6 Abstract quotient graphs for the P and D surfaces



7.2 Theory

7.2.1 Overview

Our method is two-pronged depending on whether or not a background magnetic field is present. In the absence of a magnetic field, we use singularity theory and classical geometry to classify topological features such as Dirac points and topological charges. In the presence of a magnetic field, the classical geometry becomes non-commutative. Some of the topological invariants carry over, such as a gap classification, and topological charges aka Chern classes, which could give rise to a quantum Hall effect. Some other new phenomena appear, which could potentially lead to new properties as described below.

7.2.2 Summary of the Methods

To model the electronic properties of the physical systems, we used a Harper Hamiltonian [14, 15] for the graphs described above. Physically, this corresponds to using the tight-binding approximation and Peierls substitution [16]. The system is thus modeled by the Hilbert space $\mathcal{H} = l^2(\Lambda)$, where Λ are the vertices of the graph together with the Harper Hamiltonian acting on \mathcal{H} that is given by

$$H = \sum_{i=1}^6 U_{e_i} + U_{e_i}^*$$

where the sum is over all edges e_i given above. For later generalization, we note that these edges correspond to the 6 edges of the quotient graph given in Fig. 7.2. We recall that $l^2(\Lambda)$ are the square summable series on Λ . A typical element/state is given by $\phi = (\phi)_{\lambda \in \Lambda}$ with $\phi_\lambda \in \mathbb{C}$ as complex number that can be imagined to sit at the site λ and $\sum_{\lambda \in \Lambda} |\phi_\lambda|^2 < \infty$. In the case without magnetic field U_e is the translation operator with $U_e(\phi)_\lambda = \phi_{\lambda-e}$. Its conjugate U_e^* is the translation along $-e$. In the case with magnetic field the U_e are replaced with so-called magnetic translation operators as explained in Sect. 7.3.

At this point, we wish to remark that the traditional translation operators used in absence of a magnetic field (a) commute with each other and (b) are symmetries and hence commute with the Hamiltonian, whence we call it the commutative case. In contrast, if there is a magnetic field, translations cease to commute with each other as their commutator introduces a phase. Likewise they cease to commute with the Hamiltonian. This is the origin of the non-commutative geometry.

Going back to the commutative case, using Fourier transform the operators can alternatively be considered as depending on quasi-momenta of the Brillouin zone. It is this Brillouin zone geometry that the non-commutative version also captures.

In order to present the Harper Hamiltonian as a matrix, we rewrite the Hilbert space as a direct sum $\mathcal{H} = \bigoplus_v \mathcal{H}_v$, where the sum is over the vertices v in an elementary cell, that is the vertices of the abstract quotient graphs. For instance for the gyroid \mathcal{H}_{v_0} has as elements square summable sequences $(\phi)_\lambda$ where now λ is in the sub-lattice generated by v_0 which are all the vertices v of Γ_+ that are translates of v_0 by integer linear combinations of the g_i , $i = 1, 2, 3$. Now translation along a directed edge between starting at v and ending at w will map \mathcal{H}_w to \mathcal{H}_v , by our convention.

After Fourier transform the Harper Hamiltonian becomes dependent on the quasi-momenta of the Brillouin zone. This means that we have a family of Hamiltonians depending on parameters which parameterize the Brillouin zone. For the 3d skeletal graphs this is $T^3 = S^1 \times S^1 \times S^1$, which we can visualize as a cube $[0, 2\pi]^3$ where opposite sides are identified.

We will describe the results separately for the three surfaces P, D and G.

7.2.3 The Gyroid Without Magnetic Field

There are 4 vertices in the elementary cell and accordingly in quotient graph. Hence the Hamiltonian will be a 4×4 matrix with translation operators as entries.

$$H_{\Gamma_+} = \begin{pmatrix} 0 & U_1^* & U_2^* & U_3^* \\ U_1 & 0 & U_6^* & U_5 \\ U_2 & U_6 & 0 & U_4 \\ U_3 & U_5^* & U_4^* & 0 \end{pmatrix} \quad (7.5)$$

Here we use the short hand $U_i = U_{e_i}$ and $U_i^* = U_{-e_i}$.

Using a normalization, essentially a change of basis for the lattice generators and singling out v_0 as a special vertex, by conjugation, the Harper Hamiltonian can be taken to the form [9]

$$H = \begin{pmatrix} 0 & 1 & 1 & 1 \\ 1 & 0 & A & B^* \\ 1 & A^* & 0 & C \\ 1 & B & C^* & 0 \end{pmatrix} \quad (7.6)$$

where A , B and C are combinations of translational operators of the form U_e . We refer to [9] for the details. Using Fourier transform, that is looking at states with fixed quasi-momenta, we can rewrite them as $A = \exp(ia)$, $B = \exp(ib)$, $C = \exp(ic)$, with $a, b, c \in [0, 2\pi]$ taken periodically. Alternatively, we can think of $\exp(ia)$, $\exp(ib)$ and $\exp(ic)$ as a set of generators for the functions on the 3-torus T^3 . This point of view will be generalized later.

The eigenvalues of $H(a, b, c)$, that is the energies E_i of the different bands depending on the quasi-momentum $k = (a, b, c)$ are given by the roots of the characteristic polynomial:

$$P(a, b, c, z) = z^4 - 6z^2 + a_1(a, b, c)z + a_0(a, b, c) \quad (7.7)$$

where

$$\begin{aligned} a_1 &= -2 \cos(a) - 2 \cos(b) - 2 \cos(c) - 2 \cos(a + b + c) \\ a_0 &= 3 - 2 \cos(a + b) - 2 \cos(b + c) - 2 \cos(a + c) \end{aligned}$$

The geometry of the dispersion relation, i.e. the set of the E_i as a function of the quasi-momenta $k = (a, b, c)$, is that one can view the energy spectrum as a cover of the Brillouin zone. Here over each point k of the Brillouin zone T^3 , we have the Eigenvalues of $H(k)$. Moving around k , we get a cover of T^3 which generically, i.e. when there is no degenerate Eigenvalue, has 4 sheets. There are degeneracies, however, when there are less than 4 distinct Eigenvalues and the sheets are glued together giving ramifications.

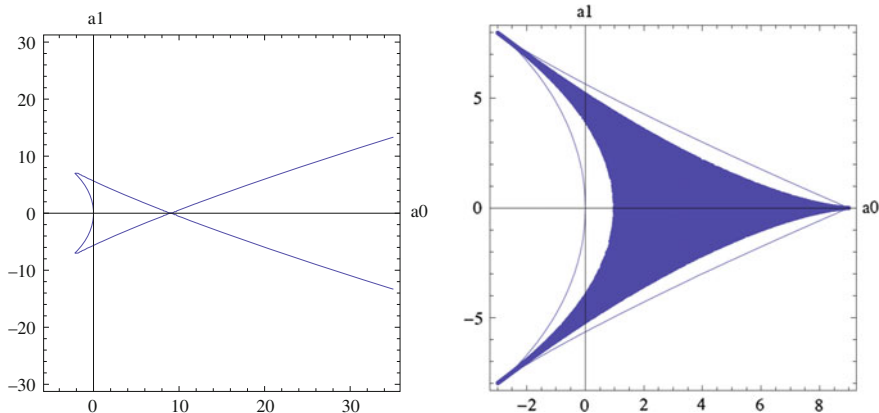


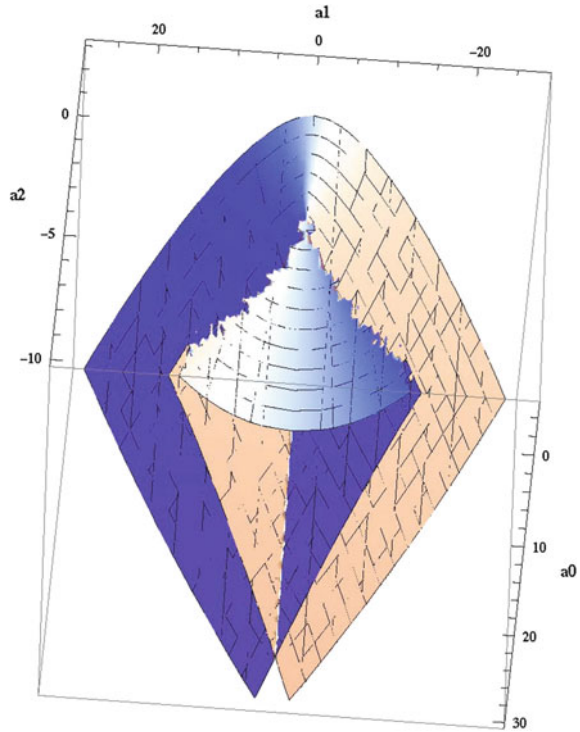
Fig. 7.7 The -6 slice of the swallowtail of A_3 and the region occupied by the gyroid

This geometry is amenable to study via singularity theory [17]. Indeed mathematically the geometry is a pull-back of a miniversal unfolding of an A -type singularity. This allowed us to analytically calculate the singular points in the gyroid spectrum and to classify them using results of Grothendieck [18].

Let us briefly highlight some of the construction. The first step is the realization that in the characteristic polynomial, the coefficients depend on the parameters (a, b, c) . Since H is traceless, there is no term of z^3 in the characteristic polynomial and we are left with the coefficients $a_i(a, b, c)$ of z^i for $i = 0, 1, 2$ with $a_2(a, b, c) = -6$ being constant. The latter fact is no coincidence, but is a consequence of the type of the graph (it is simply laced) and the fact that it has 6 edges. The miniversal unfolding of the A_3 singularity is given by the cover of the roots of the polynomial $z^4 + a_2z^2 + a_1z^1 + a_0z^0$, where now the a_i can take any complex value and are regarded as parameters. The base space of the cover is then just the parameter space of the a_i , that is \mathbb{C}^3 . Again the cover generically has 4 sheets and is ramified over the locus where some roots coincide. This locus is called the discriminant locus or the swallowtail. The second crucial observation is then that the a_i as depending on (a, b, c) define a map from the Brillouin zone to the base of the miniversal unfolding, i.e. $\mathcal{E} : T^3 \rightarrow \mathbb{C}^3$ which we called the characteristic map. Since all the values $a_i(a, b, c)$ are real, we can restrict to the real locus \mathbb{R}^3 of \mathbb{C}^3 . The spectrum of H is singular at (a, b, c) if and only if $\mathcal{E}(a, b, c)$ lies in the discriminant locus. We call these points the singular points, although, of course they are not singular in T^3 , but the cover is singular over them.

The characteristic region is the image of \mathcal{E} , that is the region that can be reached when a, b, c are varied between 0 and 2π . Since $a_2(a, b, c) = -6$, the information is captured in the a_0, a_1 plane, which should be considered as the slice at $a_2 = -6$, that is the plane parallel to the a_0, a_1 plane in \mathbb{R}^3 through $(0, 0, -6)$. This is depicted in Fig. 7.7.

Fig. 7.8 The A_3 singularity (the swallowtail)



The curve shown in the figure is the discriminant locus which is explicitly given by

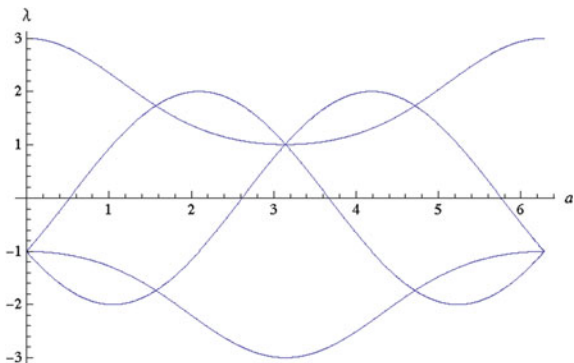
$$20736 a_0 - 4608 a_0^2 + 256 a_0^3 + 864 a_1^2 - 864 a_0 a_1^2 - 27 a_1^4 = 0 \quad (7.8)$$

As we showed, the boundaries of the characteristic region are obtained as the collection of points (a_0, a_1) for $a = b = c$ and $a = b = -c$.

The characteristic region is contained in the slice $a_2 = -6$ of the A_3 singularity (the swallowtail, shown in Fig. 7.8) and intersects the discriminant in exactly three isolated points, the two cusps and the double point of that slice of the swallowtail. This result was derived analytically.

The two cusps are in the stratum of type A_2 (where three roots coincide) and the double point is in the stratum of type (A_1, A_1) (where two pairs of roots coincide). As can be shown the fibers of \mathcal{E} over all these point are discrete giving rise to finitely many points in T^3 at which there are level crossings for the energies. For the A_2 singularities, this is just one point each at each cusp, giving rise to two triple crossings, while the fiber over (A_1, A_1) consists of two points. Over each of these points there are two double crossings and as each single crossing is of type A_1 , these are Dirac points, see below.

Fig. 7.9 Dispersion relation for the gyroid Harper Hamiltonian along the diagonal in the Brillouin zone. Note the time-reversal symmetry (TRS)



The dispersion relation (band structure) for the gyroid Harper Hamiltonian, which we calculated analytically, is shown in Fig. 7.9 along the diagonal in the Brillouin zone, that is points (a, a, a) , on which all the singular points lie.

Notice that the spectrum is symmetric under $k \rightarrow -k$, which can be read off from the Harper Hamiltonian.

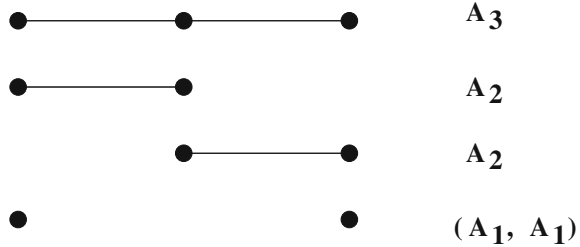
Summarizing our results for the band structure of the gyroid Harper Hamiltonian, we find two Dirac points for the gyroid at the points $(\frac{\pi}{2}, \frac{\pi}{2}, \frac{\pi}{2})$, $(\frac{3\pi}{2}, \frac{3\pi}{2}, \frac{3\pi}{2})$ in the first Brillouin zone. We have shown that at these points, the dispersion relation becomes linear [19]. They correspond to double crossings in the spectrum. These points are actually double Dirac points, i.e. there are two double crossings at each of these points. They can be seen as the 3d- analogue of Dirac points in graphene. There are further degenerate points in the spectrum at $(0, 0, 0)$ and (π, π, π) , which are triple crossings. See Fig. 7.9. All these are forced by level sticking which we found using an enhanced symmetry group of a quantum graph [20].

For a general periodic graph with n vertices in an elementary cell one again obtains a characteristic map, but now to the miniversal unfolding of A_{n-1} singularity. By a theorem of Grothendieck [18] one knows that there is a stratification of the discriminant locus obtained by deleting vertices from the A_{n-1} graphs and by also deleting any edge incident to the vertex.

For instance, in the A_3 case (see Fig. 7.8), deleting the left or right vertex leaves one with the A_2 graph and deleting the middle vertex leaves one with two copies of the A_1 graph. Hence the singularity type (A_1, A_1) , the smooth part of the swallowtail, corresponds to deleting two vertices, which gives the 3 parts of the swallowtail as strata over which there are A_1 singularities. The smallest stratum is obtained by not deleting any vertex and this is the A_3 singularity at the origin, see Fig. 7.10.

In general the singularities are then determined by the strata and the fibers of the characteristic map \mathcal{E} over the swallowtail.

Fig. 7.10 Stratification of the A_3 singularity



7.2.4 Enhanced Symmetries from a Re-gauging Groupoid

Another reason that singular points have to be present is given by symmetries, which lead to level sticking. As we will argue, the momentum space geometry is basically encoded in the quotient graph with certain decorations. In this setting local symmetries for the geometry can be induced by so-called quantum enhanced symmetries of the underlying graph. The procedure for this is not straightforward, though, and proceeds via re-gauging groupoid and a “lift” of its action to the momentum space [17]. The result of this rather elaborate process is the existence of *projective* representations of subgroups of the symmetry group of the graph that appear as stabilizers in the geometric action on the momentum space [21].

We will give a cursory overview of the calculus and refer to [17, 21] for the details. A sample graphical calculation which we now discuss is given in Fig. 7.11. This is a generalization of the methods of [22].

The main new tool we introduced refers to enhanced graph symmetries, which arise from certain re-gaugings of the Harper Hamiltonian [20]. The gauge expresses a choice of basis in which the Hamiltonian becomes a matrix whose entries lie in the same space of operators. The choice in terms of combinatorial data is given by a spanning tree and a root r for this spanning tree. The operators are then all operators on \mathcal{H}_r . We used such a gauge with $r = v_0$ to obtain the form (7.6) for the Hamiltonian. The Hamiltonian is then a decoration on the abstract graph. Basically the edge is decorated by the corresponding operator. The coefficients h_{vw} in the matrix of the Hamiltonian are then the sum over all edge decorations of the edges connecting the two vertices v and w . The gauge is reflected in the fact that the edges of the spanning tree are decorated by the identity operator 1. The first entry in Fig. 7.11 illustrates this nicely. Accordingly the entries in the first row and column of (7.6) say that the diagonal entry is 1. Acting by a symmetry of the graph moves the spanning tree and the root. This consequently breaks the gauge. For instance exchanging the vertices v_0 and v_1 of the graph yields the second entry in Fig. 7.11. In order to reestablish the gauge condition of decoration by units on the spanning tree, that is to re-gauge, one employs a decoration on the vertices, this is the third part of the figure. The vertex decorations are again by the same type of operators, which in the commutative case can be seen as phases. This decoration gives the quantum enhancement. Up to the initial condition that the root vertex is decorated by the identity, the decoration is

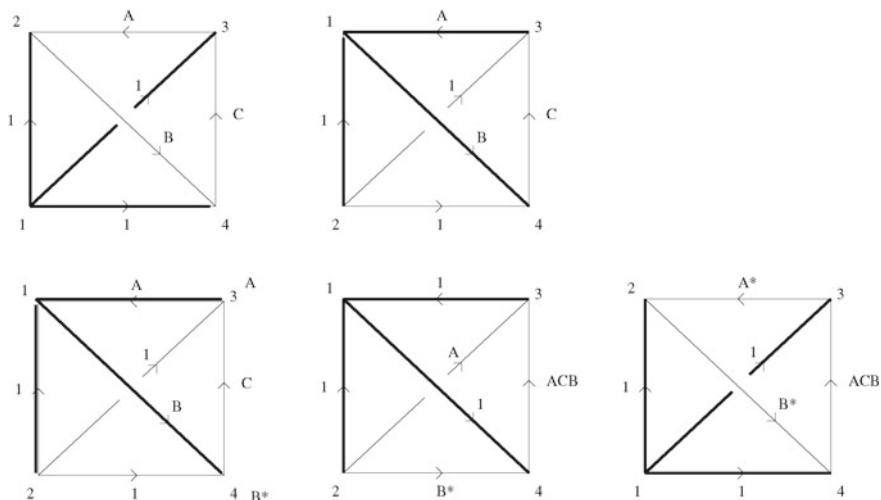


Fig. 7.11 Sample calculation of re-gauging with edge and vertex factors, see [20]

entirely determined by the two different gaugings and satisfies the requirement that when the decorations on the vertices act on the edge decoration, by multiplication from the left by the decoration of the target vertex and on the right by the conjugate of the source decoration, the decoration of the spanning tree vertices is again just by identity operators, see part four of the figure.

This type of calculation produces several bits of data. The permutation matrix, a diagonal matrix which contains the vertex factors and finally a transformation of the decorations of the edges, which in the example above is $(A, B, C) \mapsto (A^*, B^*, ACB)$. This reading off is facilitated by rewriting the abstract graph with the decorations in parallel to the original graph as shown in the last part of the figure. Regarding the A, B, C as providing coordinates (a, b, c) of T^3 the latter information gives an automorphism of T^3 . This means that to each element of the symmetry group of the finite graph, we obtain a transformation of T^3 and we can look at the stabilizer subgroups of points on T^3 . The product of the two matrices, permutation and re-gauging, then gives a *projective* representation of the stabilizer groups, which are subgroups of the symmetry group of the graph. The fact that these representations are projective is essential and this is due to the fact that we used the quantum enhanced version, which allows for re-gauging by vertex decorations.

Table 7.1 provides a nice summary of our results [20]. It shows the enhanced symmetry groups for each of the level crossings. This explains the degeneracy of each eigenvalue which is also listed in the table. It would not be possible to explain these degeneracies by the group \mathbb{S}_4 acting on the graph alone. Indeed the double Dirac point corresponds to 2-dim irreducible *projective* representations. A classical action of \mathbb{S}_4 does not have any 2-dim irreps. The projective representations can be further

Table 7.1 Possible choices of parameters (a, b, c) leading to non-Abelian enhanced symmetry groups and degenerate eigenvalues of H . Here A_4 is the alternating group and $2A_4$ its double cover which is also known as the binary tetrahedral group

a, b, c	Group	Iso class of type of extension		Dim of eigenvalues λ irreps	
$(0, 0, 0)$	S_4	S_4	Trivial	1,3	$\lambda = -1$ three times $\lambda = 3$ once
(π, π, π)	S_4	S_4	Trivializable Cocycle	1,3	$\lambda = 1$ three times $\lambda = -3$ once
$(\frac{\pi}{2}, \frac{\pi}{2}, \frac{\pi}{2})$ $(\frac{3\pi}{2}, \frac{3\pi}{2}, \frac{3\pi}{2})$	A_4	$2A_4$	Isomorphic extension	2,2	$\lambda = \pm\sqrt{3}$ Twice each

characterized by the group extension for which they form a genuine representation, see, e.g. [23].

7.2.5 Slicing, Chern Classes and Stability Under Perturbations

In order to find topological charges in 3d, we used Chern classes and a slicing method. We furthermore started to study deformations of the effective geometry and could show that the Dirac points remain effectively stable as they carry a minimal topological charge, which can be detected as jumps in the first Chern classes or the Berry phase on 2-torus slices of the 3-torus at a given height. This is shown in Fig. 7.12. The double points give jumps of 1 unit while the triple points give jumps of 2 units. Furthermore, the triple points do carry a charge, but they can split, and do so, under deformations as a numerical study shows [24]. The type of splitting can be explained if the time reversal symmetry is preserved.

The idea behind this is the following. Going back to [25, 26], we know that the integers in the integer quantum Hall effect (QHE) can be viewed as Chern numbers. Chern classes can be written as differential forms using Chern–Weil theory [27]. In particular the i th Chern class has a degree $2i$ differential form representative. Integrating the form over a $2i$ -dimensional manifold gives a number. The relevant classes here are just the first Chern classes. Here the 2-form can be thought of as the Berry curvature [26, 28]. Since the QHE is on a 2d torus, one can simply integrate over the torus. Now if we are on the 3-torus, we cannot just integrate over it. The first Chern class is a 2-form and the second Chern class would be a 4-form. On the other hand, we can look at a slice 2-torus at fixed height c and integrate the Berry curvature over just this slice. We will get one Chern number for each band. That is all the points of the form (a, b, c) , say fixed c and $a, b \in S^1 \times S^1$. In order to have the correct notion of a Berry phase, we should however have a non-degenerate

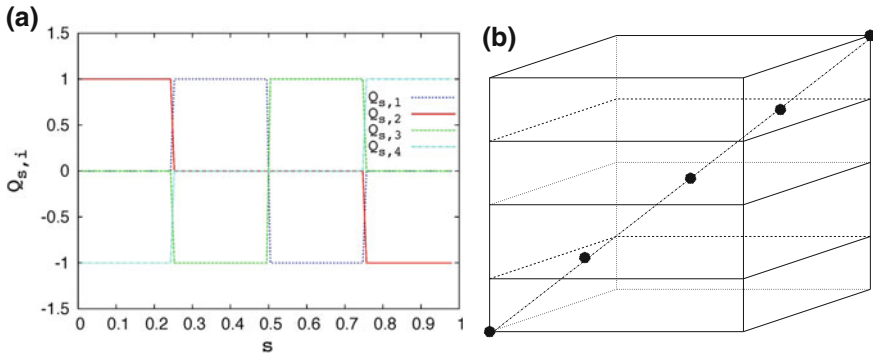


Fig. 7.12 **a** Topological charges as functions of the height of a 2-torus slice of the Brillouin zone. The jumps are step functions and the sloped transition is merely a guide. **b** The Brillouin torus as a cube with periodic boundaries, the position of the Dirac points and triple crossings along the diagonal and two 2-torus slices

Eigenvalue. So this will only work for values of c where no (a, b, c) is singular. In the gyroid example this means that $c \neq 0, \frac{\pi}{4}, \frac{\pi}{2}, \frac{3\pi}{4}$. In this way, we get the Chern number of the i th band as a function of c as a well defined integer outside these special values of c . Since the Chern number is a topological invariant, it is locally constant. It does, however, jump when c crosses one of the bad points above. This jump depends on the local structure of the singularity. It is by ± 1 for Dirac points, but can be more complicated for more complicated singularities. We determined the local structure over the A_2 singular triple crossing points, which told us that the jumps are by $-2, 0, 2$ for the three crossing bands. The numerical check is depicted in the first part of Fig. 7.12, while the second part of the figure shows the slices in four regions of constant Chern classes.

What is special in 3-d is that these charges are now protected in the sense that under perturbations, more singular points may appear, but the net jump over these points is conserved. Numerically we found that the double Dirac points drift apart, while the triple crossings decay into four double crossings under deformations that preserve the time reversal symmetry that is present in the original context [24].

We showed [17] that slicing in all three directions actually totally fixes the homological information obtainable from Berry phases and curvature.

7.2.6 Possible Experimental Verification

It would be intriguing to measure the Dirac cones in this particularly rich 3d geometry experimentally. There are two hurdles that have to be overcome. First, one has to find a material with the right Fermi surface, but this should be possible. The second is that these Dirac points are buried in the continuum, since cutting at this particular energy

will form actual Fermi surfaces away from the Dirac points. This type of investigation has been done, however, in topological semimetals [29, 30] using angle-resolved photoemission spectroscopy (ARPES). The Dirac points for the gyroid lie along the diagonal slice of the Brillouin zone and it should be possible to find a curve through them that has a pseudo-gap.

A similar study has been performed in photonics [31] using angle resolved transmission measurement.

Moreover, the Dirac points are stable under symmetry breaking deformations [17, 24] and hence give affirmation of the applicability of the theory to real materials. Perhaps these effects, including the decay of the higher order singularity, can be used advantageously. Mathematically there are associated topological charges stemming from first Chern classes. These manifest themselves as jumps in the first Chern classes or the integral over the Berry curvature on 2-torus slices. It would also be very interesting to measure the decay of the triple points that is predicted by global constraints. Finding the triple points in the 3d material experimentally would be a great step in realizing properties forced by interesting topology.

Let us now briefly mention the results for the other geometries:

7.2.7 *The P Wire Network Without Magnetic Field*

It can be shown that the characteristic polynomial is simply a polynomial of degree 1 [19], $P(t, z) = z - \sum_i t_i$, so that after shifting z we are left with just $z = 0$, which is not critical. Not surprisingly, there are no singularities. That means that the cover itself is just the trivial cover of T^3 by itself. Nevertheless the slice geometry is that of T^2 which supports the quantum Hall effect. Accordingly this example becomes interesting in the presence of a magnetic field.

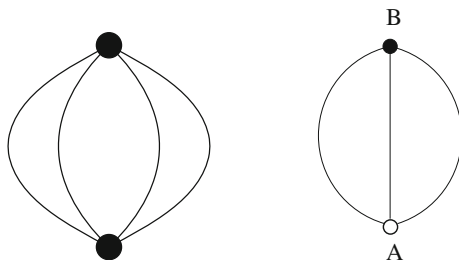
In terms of representations, there is only the root of the spanning tree which is unique. The S_3 action permutes the edges and their weights. This yields the permutation action on the T^3 . There is no nontrivial cover and the eigenvalues remain invariant.

7.2.8 *The D Wire Network and the Honeycomb Lattice Without Magnetic Field*

We treat the diamond and the honeycomb case in parallel since they have similar quotient graphs. The graphs $\tilde{\Gamma}$ are given in Fig. 7.13. The honeycomb lattice is used to model graphene, and indeed we reproduce the known results about Dirac points in graphene with our theory. This is a nice cross-check.

After gauging, the Hamiltonians are

Fig. 7.13 The graphs $\bar{\Gamma}$ for the diamond (left) and the honeycomb case (right)



$$H_{hon} = \begin{pmatrix} 0 & 1 + U + V \\ 1 + U^* + V^* & \end{pmatrix} \tag{7.9}$$

and

$$H_D = \begin{pmatrix} 0 & 1 + U + V + W \\ 1 + U^* + V^* + W^* & \end{pmatrix} \tag{7.10}$$

We use $U = \exp(iu)$, $V = \exp(iv)$, $W = \exp(iw)$ with u, v, w real. The fact that there are sums in the entries is due to the fact that there are multiple edges connecting the two vertices.

The polynomials are $P(u, v, z) = z^2 - 3 - 2\cos(u) - 2\cos(v) - 2\cos(u - v)$ and $P(u, v, w, z) = z^2 - 4 - 2\cos(u) - 2\cos(v) - 2\cos(w) - 2\cos(u - v) - 2\cos(u - w) - 2\cos(v - w)$. The characteristic regions in \mathbb{R} are just the intervals $[-9, 0]$ and $[-16, 0]$. The discriminant is the point 0. From this we see that in both cases we have to have $a_0 = 0$ and the singular locus is simply this fiber.

7.2.8.1 The Honeycomb Case

For the honeycomb, the standard calculation shows that if $a_0 = 0$ then $U = V^*$ and $U \in \{\rho_3 := \exp(2\pi i/3), \bar{\rho}_3\}$, which means that the fiber consists of 2 points. These are the well known Dirac points $(\rho_3, \bar{\rho}_3)$, $(\bar{\rho}_3, \rho_3)$.

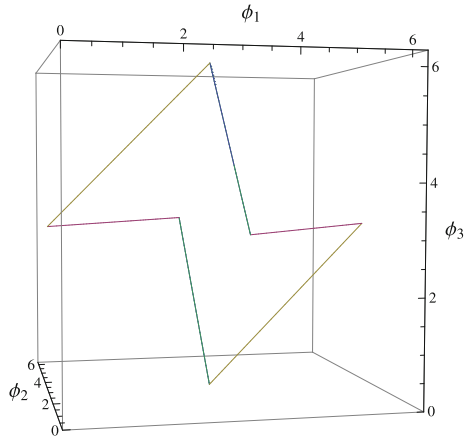
In terms of representations, we can look at the graph symmetries which are combinations of the interchange of the two vertices or the three edges (see Fig. 7.13). The vertex interchange renders the fixed points $u = \pm 1, v = \pm 1$ which have eigenvectors $v_1 = (1, 1)$ and $v_2 = (-1, 1)$ and eigenvalues $1 + u + v$ and $-(1 + u + v)$, respectively. The irreps of the C_3 action are $triv \oplus \omega$ where $\omega = \exp(\frac{2i\pi}{3})$.

As far as the edge permutations are concerned the interesting one is the cyclic permutation (123) which yields the equations

$$u = \bar{v}, v = \bar{v}u$$

for fixed points. Hence $u^3 = 1$. We get non-trivial matrices at the two points $(\omega, \bar{\omega})$ and $(\bar{\omega}, \omega)$. At these points e_1, e_2 are eigenvectors with eigenvalue 0 and $H = 0$, since $1 + u + v = 1 + \omega + \bar{\omega} = 0$.

Fig. 7.14 The 3-torus as a cube with opposite sides identified and the singular locus of the diamond locus consisting of three circles pairwise intersecting in a point



Denoting the elements of $\mathbb{Z}/2\mathbb{Z}$ again by $+$, $-$, there is an embedding of $\mathbb{S}_3 \rightarrow \mathbb{Z}/2\mathbb{Z} \times \mathbb{S}_3$ given by $(12) \mapsto (-, (12)), (23) \mapsto (-, (23))$. Notice that $(123) \mapsto (+, (123))$. It is then an easy check that the equations for the fixed points are satisfied exactly by $(\omega, \bar{\omega})$ and $(\bar{\omega}, \omega)$. The representation is a projective representation of \mathbb{S}_3 cohomologous to the 2-dim irreducible representation of \mathbb{S}_3 .

The fixed points are exactly the Dirac points of graphene and the symmetry above forces the degeneracies.

7.2.8.2 The Diamond Case

The equation for the fiber over 0,

$$-4 - 2\cos(u) - 2\cos(v) - 2\cos(w) - 2\cos(u - v) - 2\cos(u - w) - 2\cos(v - w) = 0$$

has been solved in [19] and the solutions are given by $(u, v, w) = (\phi_i, \phi_j, \phi_k)$ with $\phi_i = \pi, \phi_j \equiv \phi_k + \pi \pmod{2\pi}$ with $\{i, j, k\} = \{1, 2, 3\}$. So in this case the fiber of the characteristic map is 1-dimensional and the pull-back has singularities along a locus of dimension 1, which also implies that there are no Dirac points. Geometrically the singular locus are three circles pairwise intersecting in a point. This is shown in Fig. 7.14.

Looking at representations, things again become interesting. Permuting the two vertices, we obtain eight fixed points if $u, v, w \in \{1, -1\}$. The matrix for this transposition is $\begin{pmatrix} 0 & 1 \\ 1 & 0 \end{pmatrix}$. This gives super-selection rules and we know that $v_1 = (1, 1)$ and $v_2 = (-1, 1)$ are eigenvectors. The eigenvalues being $1 + u + v + w$ and $-(1 + u + v + w)$ at these eight points.

We can also permute the edges with the \mathbb{S}_4 action. In this case the \mathbb{S}_3 action leaving the spanning tree edge invariant acts as a permutation on (u, v, w) . The

relevant matrices however are just the identity matrices and the representation is trivial. The transposition (12), however, results in the action $(u, v, w) \mapsto (\bar{u}, \bar{u}v, \bar{u}w)$ on T^3 , see Fig. 7.11. So to be invariant we have $u = 1$, but this implies that ρ_{12} is the identity matrix. Invariance for (13) and (14) and the three cycles containing 1 are similar. But, if we look at invariance under the element (12)(34) we are lead to the equations $u = \bar{u}$, $v = \bar{u}w$, $w = \bar{u}v$. This has solutions $u = 1$, $v = w$, for these fixed points again we find only a trivial action. But for $u = -1$, $v = -w$ these give rise to the diagonal matrix $diag(1, -1)$ and hence eigenvectors $e_1 = (1, 0)$ and $e_2 = (0, 1)$, but looking at the Hamiltonian, these are only eigenvectors if it is the zero matrix $H(u, v, w) = 0$. Indeed the conditions above imply $1 + u + v + w = 0$. Similarly, we find a $\mathbb{Z}/2\mathbb{Z}$ group for (13)(24) and (14)(23) yielding the symmetric equations $v = -1$, $u = -w$ and $w = -1$, $u = -v$. These are exactly the three circles found in [13].

Going to bigger subgroups of \mathbb{S}_4 we only get something interesting if the stabilizer group G_t contains precisely two of the double transpositions above. That is the Klein four group $\mathbb{Z}/2\mathbb{Z} \times \mathbb{Z}/2\mathbb{Z}$. The invariants are precisely the intersection points of the three circles given by $u = v = -1$ and $w = 1$ and its cyclic permutations.

To find the 2-dimensional irreducible representations, we look at different Klein four groups embedded into $\mathbb{Z}/2\mathbb{Z} \times \mathbb{S}_4$. If we denote the elements of $\mathbb{Z}/2\mathbb{Z}$ by $+$, $-$, then we first look at $(+, id)$, $(+, (12)(34))$, $(-, (13)(24))$, $(-, (14)(23))$. The element $(-, (13)(24))$ is the composition of edge permutation (13)(24) together with the switching of the vertices. It gives the equation $u = v\bar{w}$ for fixed points, while the fixed points of $(-, (14)(23))$ satisfy $u = \bar{v}w$. Combining these equations with the ones for (12)(23) above, we find again the solutions $u = 1$, $v = w$ and $u = -1$, $v = -w$. The difference however is that the representation in the case $u = -1$ is the irreducible projective representation of the Klein group corresponding to the irreducible 2-dim representation of its 2-fold cover given by the quaternion group $\pm 1, \pm i, \pm j, \pm k$. For $u = 1$ the irreps are one-dimensional and give no new information. Using the different embeddings of the Klein group we find the 2-dim irreps on the three circles above responsible for the degeneration of the eigenvalues. These are three lines of doubly degenerate eigenvalue 0. They are not Dirac points since there is one free parameter accordingly the fibers of the characteristic map of [19] are one dimensional which implies that the singular point is not isolated.

Additional cases of planar graphs that do not correspond directly to CMC surfaces are discussed in [19]. We do not find any Dirac points, either. So the gyroid remains the only object in this family of 3-d wire networks from CMC surfaces that exhibits 3-d Dirac points.

7.3 Noncommutative Approach in the Presence of a Magnetic Field

In the case with magnetic field, we used an approach from non-commutative geometry [32–34]. Here the geometry is modeled by a C^* -algebra \mathcal{B}_Θ , which is the smallest algebra containing the Hamiltonian and the translational symmetries. The standard choice of the Hamiltonian is again the Harper Hamiltonian [9] above, but where now the U_e are replaced by so called magnetic translation operators, which do not commute, but satisfy

$$U_{e_1}U_{e_2} = \exp\left(\int_R B dS\right)U_{e_2}U_{e_1},$$

where R is the rectangle spanned by the two vectors e_1 and e_2 . The aim is then to classify the algebras \mathcal{B}_Θ that appear when the magnetic field is varied. There Θ is the magnetic field parameter. The magnetic fields we considered were constant magnetic fields, so that there are three real parameters for the coefficients of the field. We often use the quadratic form $\hat{\Theta}$ corresponding to the B -field $B = 2\pi\hat{\Theta}$.

The basic ingredients are like in the commutative case. We can gauge by picking a vertex and a spanning tree, so that the decorations along the spanning tree and hence the entries in the Hamiltonian are 1. The other decorations are now some combinations of magnetic translation operators. It turns out, as we showed, that these operators satisfy the relations of a non-commutative torus, so that the Hamiltonian becomes a matrix with coefficients in the non-commutative torus.

In particular for the gyroid, we are dealing with the non-commutative 3-torus. By definition the non-commutative 3-torus \mathbb{T}_Θ^3 is the C^* algebra spanned by 3 linearly independent unitary operators O_i that satisfy the commutation relations $O_iO_j = \exp(2\pi i\theta_{ij})O_jO_i$ for $i, j, k = 1, 2, 3$, where θ_{ij} is a skew-symmetric matrix determined by the magnetic field. The operators in question are the A, B, C of (7.6), which now just do not commute anymore. The relation to the classic commutative geometry is given by the fact that the commutative unital C^* algebra of continuous complex valued functions on \mathbb{T}_Θ^3 , that is $C^*(\mathbb{T}_\Theta^3) = C(\mathbb{T}_\Theta^3, \mathbb{C})$ is the C^* algebra generated by the three functions $\exp(ia), \exp(ib), \exp(ic)$. The lattice translations can also be written as matrices with entries in the non-commutative 3-torus. Thus the algebra \mathcal{B}_Θ is isomorphic to a subalgebra of the C^* algebra of 4×4 matrices with coefficients in the non-commutative (nc) 3-torus.

The inclusion of the nc 3-torus into the algebra \mathcal{B}_Θ as the lattice translations is by definition the nc geometry based on the gyroid in a magnetic field. It captures the non-commutative deformation of the Eigenvalue cover of the Brillouin zone in the previous discussion. To make the connection, we recall that in general a covering map is a special type of surjection $\pi : E \rightarrow B$ which when we regard functions yields a pull-back map going the other way around: $\pi^* : C^*(B) \rightarrow C^*(E)$ which sends a function f on B to the function $f \circ \pi$ on E . In our case $B = \mathbb{T}_\Theta^3$ the Brillouin zone and E is the cover by the Eigenvalues aka energies.

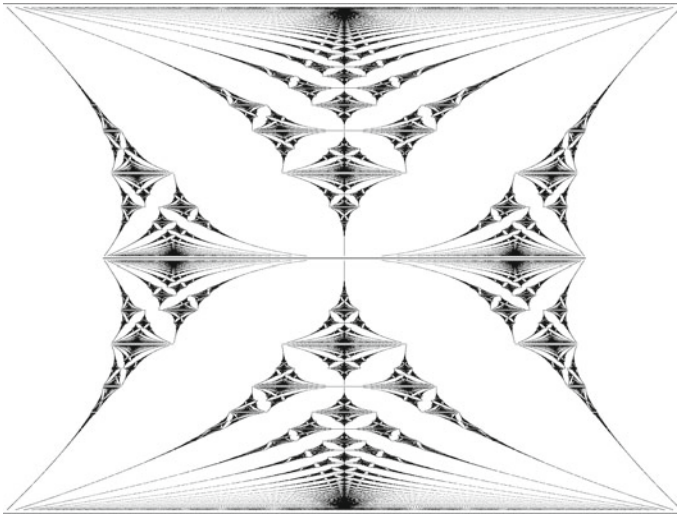


Fig. 7.15 Hofstadter's butterfly; the image shows the distribution of energy levels E of Bloch electrons in a magnetic field in 2 dimensions [36]

An upshot of this theory is that some of the methods, like Chern-classes and K-theory, that is the theory of bundles with addition and formal difference, carry over to this setting.

7.3.1 Gyroid in the Presence of a Magnetic Field

There are two series of results. Based on a rather abstract K-theoretic argument following [33], our study predicts a distribution of energy gaps in the gyroid spectrum in terms of the magnetic field that is a 3-d analogue of Hofstadter's butterfly [35], which results in the 2d setting for the Bravais lattice \mathbb{Z}^2 , see Fig. 7.15. To be more precise, if the magnetic field is a fixed 3-dim vector, for rational values of the magnetic field, there are finitely many gaps, for irrational values there are possibly infinitely many gaps. This is a very interesting result that has not yet been checked experimentally to our knowledge.

The second series of results characterizes the abstract algebra \mathcal{B}_Θ . Our calculations lead to the following conclusions: The algebra \mathcal{B}_Θ is generically the full matrix algebra and hence Morita equivalent to the non-commutative 3-torus. It is true sub-algebra only at finitely many rational points in the parameter space given by the three parameters of the magnetic field, which we listed explicitly [9]. We will express the results here in terms of the bcc lattice vectors given in (7.2). B represents the 3-dimensional vector of a constant magnetic field. We define the following parameters:

$$\theta_{12} = \frac{1}{2\pi} B \cdot (g_1 \times g_2), \quad \theta_{13} = \frac{1}{2\pi} B \cdot (g_1 \times g_3), \quad \theta_{23} = \frac{1}{2\pi} B \cdot (g_2 \times g_3)$$

$$\alpha_1 := e^{2\pi i \theta_{12}} \bar{\alpha}_2 := e^{2\pi i \theta_{13}} \alpha_3 := e^{2\pi i \theta_{23}}$$

$$\phi_1 = e^{\frac{\pi}{2} i \theta_{12}}, \quad \phi_2 = e^{\frac{\pi}{2} i \theta_{31}}, \quad \phi_3 = e^{\frac{\pi}{2} i \theta_{23}}, \quad \Phi = \phi_1 \phi_2 \phi_3$$

Our results can then be summarized as follows:

1. If $\Phi \neq 1$ or not all α_i are real then $\mathcal{B}_\Theta = M_4(\mathbb{T}_\Theta^3)$.
2. If $\Phi = 1$, all $\alpha_i = \pm 1$, at least one $\alpha_i \neq 1$ and all ϕ_i are different then $\mathcal{B}_\Theta = M_4(\mathbb{T}_\Theta^3)$.
3. If $\phi_i = 1$ for all i then the algebra is the same as in the commutative case.
4. In all other cases (this is a finite list) \mathcal{B} is non-commutative and $\mathcal{B}_\Theta \subsetneq M_4(\mathbb{T}_\Theta^3)$.

It would be very interesting to find and measure special properties of a corresponding material at these values of the magnetic field. There should be a hidden symmetry or charge associated to the reduction of the algebra to a proper sub-algebra.

7.3.2 *P Wire Network in a Magnetic Field*

For the simple cubic lattice (and also any other Bravais lattice of rank k , the simple cubic lattice has $k = 3$): if $\Theta \neq 0$ then \mathcal{B}_Θ is simply the noncommutative torus \mathbb{T}_Θ^k and if $\Theta = 0$ then this \mathcal{B}_0 is the C^* algebra of T^k . There are no degenerate points.

The analysis of [14] of the quantum Hall effect, however, suggests that there is a non-trivial noncommutative line bundle in the case of $k = 2$ for *non-zero B-field*. Furthermore, in this case there is a non-trivial bundle, not using the noncommutative geometry, but rather the Eigenfunctions constructed in [25] for the full Hilbert space \mathcal{H} . This is what is also considered in [26].

7.3.3 *D Wire Network in a Magnetic Field*

We express our results in terms of parameters q_i and χ_i defined as follows: Set $e_1 = \frac{1}{4}(1, 1, 1)$, $e_2 = \frac{1}{4}(-1, -1, 1)$, $e_3 = \frac{1}{4}(-1, 1, -1)$. For $B = 2\pi \Theta$ let

$$\Theta(-e_1, e_2) = \varphi_1 \quad \Theta(-e_1, e_3) = \varphi_2 \quad \Theta(e_2, e_3) = \varphi_3 \quad \text{and} \quad \chi_i = e^{i\varphi_i} \quad \text{for } i = 1, 2, 3 \quad (7.11)$$

There are three operators U, V, W , given explicitly in [13], which span \mathbb{T}_Θ^3 and have commutation relations

$$UV = q_1 VU \quad UW = q_2 WU \quad VW = q_3 WV \quad (7.12)$$

where the q_i expressed in terms of the χ_i are:

$$q_1 = \bar{\chi}_1^2 \chi_2^2 \chi_3^2 \quad q_2 = \bar{\chi}_1^6 \bar{\chi}_2^2 \bar{\chi}_3^2 \quad q_3 = \bar{\chi}_1^2 \bar{\chi}_2^6 \bar{\chi}_3^2 \quad (7.13)$$

Vice versa, fixing the values of the q_i fixes the χ_i up to eighth roots of unity:

$$\chi_1^8 = \bar{q}_1 \bar{q}_2 \quad \chi_2^8 = q_1 \bar{q}_3 \quad \chi_3^8 = q_1^2 \bar{q}_2 q_3 \quad (7.14)$$

Other useful relations are $q_2 \bar{q}_3 = \bar{\chi}_1^4 \chi_2^4 \bar{\chi}_3^4$ and $q_2 q_3 = \bar{\chi}_1^8 \bar{\chi}_2^8$. The algebra \mathcal{B}_Θ is the full matrix algebra *except* in the following cases in which it is a proper subalgebra.

1. $q_1 = q_2 = q_3 = 1$ (the special bosonic cases) and one of the following is true:
 - a. All $\chi_i^2 = 1$ then \mathcal{B}_Θ is isomorphic to the commutative algebra in the case of no magnetic field above.
 - b. Two of the $\chi_i^4 = -1$, the third one necessarily being equal to 1.
2. If $q_i = -1$ (special fermionic cases) and $\chi_i^4 = 1$. This means that either
 - a. all $\chi_i^2 = -1$ or
 - b. only one of the $\chi_i^2 = -1$ the other two being 1.
3. $\bar{q}_1 = q_2 = q_3 = \bar{\chi}_2^4$ and $\chi_1^2 = 1$ it follows that $\chi_2^4 = \chi_3^4$. This is a one parameter family.
4. $q_1 = q_2 = q_3 = \bar{\chi}_1^4$ and $\chi_2^2 = 1$ it follows that $\chi_1^4 = \bar{\chi}_3^4$. This is a one parameter family.
5. $q_1 = q_2 = \bar{q}_3 = \bar{\chi}_1^4$ and $\chi_1^2 = \bar{\chi}_2^2$. It follows that $\chi_3^4 = 1$. This is a one parameter family.

The same remark as made above for the gyroid geometry applies. In this case there is an even more interesting structure that appears in the phase diagram of algebras.

7.3.4 Honeycomb in a Magnetic Field

Generically $\mathcal{B}_\Theta = \mathbb{T}_\Theta^2$. In order to give the degenerate points, let $-e_1 := (1, 0)$, $e_2 = \frac{1}{2}(1, \sqrt{3})$, $e_3 := \frac{1}{2}(1, -\sqrt{3})$ be the lattice vectors and $f_2 := e_2 - e_1 = \frac{1}{2}(-3, \sqrt{3})$, $f_3 := e_3 - e_1 = \frac{1}{2}(3, \sqrt{3})$ the period vectors of the honeycomb lattice. The parameters we need are

$$\theta := \hat{\Theta}(f_2, f_3), \quad q := e^{2\pi i \theta} \quad \text{and} \quad \phi = \hat{\Theta}(-e_1, e_2), \quad \chi := e^{i\pi \phi}, \quad \text{thus} \quad q = \bar{\chi}^6 \quad (7.15)$$

where $\hat{\Theta}$ is the quadratic form corresponding to the B -field $B = 2\pi \hat{\Theta}$.

Our results can be summarized as follows:

The algebra \mathcal{B}_Θ is the full matrix algebra of $M_2(\mathbb{T}_\Theta^2)$ except in the following finite list of cases [9]

1. $q = 1$.
2. $q = -1$ and $\chi^4 = 1$.

The precise algebras are given in [9]. We wish to point out that $q = \chi = 1$ is the commutative case and $q = -\chi = 1$ is isomorphic to the commutative case, while the other cases give non-commutative proper subalgebras of $M_2(\mathbb{T}_0^2)$.

7.3.5 Possible 3d Quantum Hall Effect

Another consequence is that with a suitable material the gyroid channels should exhibit a 3-d quantum Hall effect. The 3-d quantum Hall effect has been predicted in different materials from isotropic 3-d crystals to layered structures like graphite. The gyroid system will be particularly well suited to experimental access given that it is a super-lattice and has a large lattice constant. With the lattice constant being this large, the magnetic field required to observe the quantum Hall effect will be in a normal range (see the discussion in [37]). Indeed the quantum Hall effect for the graphene type lattice was realized at 13–14 nm [38].

Another interesting research direction is provided by the nc geometry of the gyroid in a constant magnetic field which manifests itself in a type of phase diagram. For generic values of the magnetic field, the effective non-commutative geometry (nc) is that of the nc 3-torus. However, there are certain families parameterized by special values of the magnetic field such that the unit fluxes are particularly tuned, which correspond to different geometries. It would be exciting to find special behavior of the materials at these values. The different geometries could entail further topological quantum numbers, such as those corresponding to the QHE.

7.4 General Theory and Possible Material Design

So far, we have discussed how to start from a real world structure such as a periodic wire network and obtain properties from its topology via the use of graphs. In the end, everything devolved to having a finite graph with decorations. We can reverse this question. Can one construct materials from the finite graph and what properties are then forced by this? First, one will have to find a periodic graph Γ in real space \mathbb{R}^d , which is a cover of the finite graph $\bar{\Gamma}$. This means that $\bar{\Gamma} = \Gamma/\mathbb{Z}^d$ where \mathbb{Z}^d is the translational symmetry group. By covering theory [39], we can construct such a cover for each normal subgroup of the fundamental group of Γ . Since Γ is connected, the fundamental group is the free group \mathbb{F}_b where b is the Betti number of the graph $\bar{\Gamma}$. This is the number of independent loops, which has the following two interpretations. If we take a spanning tree of $\bar{\Gamma}$ and contract it, we are left with a graph with one vertex and b loops. More technically b is the rank of the first homology group $H_1(\bar{\Gamma})$. By general covering theory [39] there is a cover Γ_N of $\bar{\Gamma}$ for each normal subgroup

$N \subset \mathbb{F}_b$, such that $\bar{\Gamma} = \Gamma_N/(G/N)$. In our case, we are thus looking for normal subgroups N of \mathbb{F}_b such that $\mathbb{F}_b/N \simeq \mathbb{Z}^b$. One choice for N , which yields the so called maximal Abelian cover is the commutator subgroup $[\mathbb{F}_b, \mathbb{F}_b] \subset \mathbb{F}_b$. Modding out by the commutators makes the free group \mathbb{F}_b into the free Abelian group \mathbb{Z}^b . There are other smaller covers with the desired property as well.

Following [40, 41] the abstract maximal Abelian cover Γ can actually be embedded as a graph $\Gamma \subset \mathbb{R}^{b_1} \simeq H_1(\bar{\Gamma}, \mathbb{R})$ with \mathbb{Z}^{b_1} acting on the ambient \mathbb{R}^{b_1} inducing the covering action on Γ . This graph is called canonical placement and has an energy minimizing property.

With certain assumptions that are called fully commutative toric non-degenerate case in [20], we can reconstruct all the data from the finite graph using the maximal Abelian cover. This is the case for our examples. For the smaller covers one also needs an embedding $N \subset \mathbb{F}_b$ which has to satisfy certain conditions. One can go one step further to the nc case as well by adding abstract operators along the edges, and then generating a C^* algebra with them by forcing certain commutation relations. For example, use a spanning tree, then each edge in the graph not in the spanning tree is decorated with an operator O_e and these operators are chosen to generate the b -dim non-commutative torus (this is essentially the toric non-degenerate case). There are more possibilities here as well.

A systematic study of such decorated graphs and their quantum enhanced symmetry groups could be used for material design. The cover will tell one which structure to construct in real space and the quantum symmetry groups will then force degeneracies such as Dirac cones.

7.5 Discussion and Conclusion

We have treated three cases of wire networks stemming from minimal CMC surfaces as well as the honeycomb lattice underlying graphene in the context of a Harper Hamiltonian on an abstract quotient graph. We were able to derive level crossings in the band structure analytically and characterize them completely using methods from singularity theory and representation theory. This leads to a complete theoretical understanding of all degeneracies in the spectra. Among other results, we showed that the gyroid wire network is the only geometry exhibiting isolated Dirac points in 3d. In the presence of a magnetic field, we proposed a new approach from non-commutative geometry that characterizes the spectrum for the gyroid wire network as 3d analogue of Hofstadter's butterfly and leads to a classification of the abstract algebra \mathcal{B}_Θ . Combined with specific material dependent properties and knowledge about the Fermi level, we expect that this leads to new results and predictions about a possible phase diagram. Let us briefly discuss the series of results that may be relevant for an experimentalist. The gyroid wire network is a new, complex system that could exhibit a 3-d quantum Hall effect and provide a fractal Hofstadter butterfly, much like a 3d analog of graphene. Furthermore it has a modified behavior at special parameters of the magnetic field. Without magnetic field, again parallel to graphene,

the gyroid has a linear dispersion relation at its Dirac points, which are additionally protected by topological charges. The feasibility of these speculations comes from the synthesis of this material at the 18 nm scale, which constitutes a super-lattice that affords the necessary fluxes.

We furthermore propose to use the present study as the starting point to design specific materials that have desired properties. We argue that it is sufficient to impose constraints on the abstract finite quotient graph to obtain them in the full lattice structure. This could be a very powerful method.

More generally our methods apply to a wide range of periodic systems and can be expanded to other lattices and geometries.

Acknowledgements BK thankfully acknowledges support from the NSF under the grants PHY-0969689 and PHY-1255409. RK thanks the Simons Foundation for support under the collaboration grant #317149.

References

1. D.M. Anderson, H.T. Davis, J.C.C. Nitsche, L.E. Scriven, *Adv. Chem. Phys.* **77**, 337–396 (1990)
2. H.A. Schwarz, *Gesammelte Mathematische Abhandlungen*, vol. I (Springer, Berlin, 1890)
3. A.H. Schoen, NASA TN-D5541 (1970)
4. T. Hahn (ed.), *International Tables for Crystallography*, vol. A (Springer, Berlin, 2005)
5. K.A. Brakke, *Exp. Math.* **1**, 141–165 (1992)
6. C.A. Lambert, L.H. Radzilowski, E.L. Thomas, Curved surfaces in chemical structure. *Philos. Trans. Math. Phys. Eng. Sci.* **354**(1715), 2009–2023 (1996)
7. V.N. Urade, T.C. Wei, M.P. Tate, H.W. Hillhouse, *Chem. Mater.* **19**(4), 768–777 (2007)
8. K. Michielsen, D.G. Stavenga, *J. R. Soc. Interface* **5**, 85–94 (2008)
9. R.M. Kaufmann, S. Khlebnikov, B. Wehefritz-Kaufmann, *J. Noncommutative Geom.* **6**, 623–664 (2012)
10. K. Große-Brauckmann, M. Wohlgemuth, *Calc. Var.* **4**, 499–523 (1996)
11. E. Stach, Private communication
12. S. Khlebnikov, H.W. Hillhouse, *Phys. Rev. B* **80**(11), 115316 (2009)
13. R.M. Kaufmann, S. Khlebnikov, B. Wehefritz-Kaufmann, *J. Phys. Conf. Ser.* **343**, 012054 (2012)
14. J. Bellissard, A. van Elst, H. Schulz-Baldes, *J. Math. Phys.* **35**, 5373–5451 (1994)
15. M. Marcolli, V. Mathai, Towards the fractional quantum Hall effect: a noncommutative geometry perspective, in *Noncommutative Geometry and Number Theory: Where Arithmetic Meets Geometry*, ed. by Caterina Consani, Matilde Marcolli (Vieweg, Wiesbaden, 2006), pp. 235–263
16. G. Panati, H. Spohn, S. Teufel, *Commun. Math. Phys.* **242**, 547–578 (2003)
17. R.M. Kaufmann, S. Khlebnikov, B. Wehefritz-Kaufmann, *J. Singul.* **15**, 53–80 (2016)
18. M. Demazure, Classification des germes à point critique isolé et à nombres de modules 0 ou 1 (d’après Arnol’d). *Séminaire Bourbaki*, 26e année, vol. 1973/74 Exp. No 443, pp. 124–142, *Lecture Notes in Mathematics*, vol. 431 (Springer, Berlin, 1975)
19. R.M. Kaufmann, S. Khlebnikov, B. Wehefritz-Kaufmann, *Ann. Phys.* **327**, 2865–2884 (2012)
20. R.M. Kaufmann, S. Khlebnikov, B. Wehefritz-Kaufmann, *Ann. Henri Poincaré* **17**, 1383–1414 (2016)
21. R.M. Kaufmann, S. Khlebnikov, B. Wehefritz-Kaufmann, *J. Phys. Conf. Ser.* **597**, 012048 (2015)
22. J.E. Avron, A. Raveh, B. Zur, *Rev. Mod. Phys.* **60**, 873 (1988)

23. G. Karpilovsky, *Projective Representations of Finite Groups* (Dekker, New York, 1985)
24. R.M. Kaufmann, S. Khlebnikov, B. Wehefritz-Kaufmann, Topologically stable Dirac points in a three-dimensional supercrystal, in preparation
25. D.J. Thouless, M. Kohmoto, M.P. Nightingale, M. den Nijs, *Phys. Rev. Lett.* **49**, 405–408 (1982)
26. B. Simon, *Phys. Rev. Lett.* **51**, 2167–2170 (1983)
27. D. Husemöller, *Fibre Bundles*, vol. 20, Graduate Texts in Mathematics (Springer, Berlin, 1993)
28. M.V. Berry, *Proc. R. Soc. Lond. A* **392**, 45–57 (1984)
29. S.-Y. Xu et al., *Science* **347**, 294 (2015)
30. B.-J. Yang, N. Nagaosa, *Nat. Commun.* **5**, 4898 (2014)
31. L. Lu, L. Fu, J.D. Joannopoulos, M. Soljacic, *Nat. Photonics* **7**, 294–299 (2013)
32. A. Connes, *Noncommutative Geometry* (Academic Press Inc., San Diego, 1994)
33. J. Bellissard, *From Number Theory to Physics* (Springer, Berlin, 1992), pp. 538–630
34. P.G. Harper, *Proc. Phys. Soc. Lond. A* **68**, 874–878 (1955)
35. D.R. Hofstadter, *Phys. Rev. B* **14**(1976), 2239–2249 (1976)
36. D. Weiss, *Nat. Phys.* **9**, 395–396 (2013)
37. M. Koshino, H. Aoki, *Phys. Rev. B* **67**, 195336 (2003)
38. C.R. Dean, L. Wang, P. Maher, C. Forsythe, F. Ghahari, Y. Gao, J. Katoch, M. Ishigami, P. Moon, M. Koshino, T. Taniguchi, K. Watanabe, K.L. Shepard, J. Hone, P. Kim, *Nature* **497**, 598 (2013)
39. J.R. Munkres, *Topology: A First Course* (Prentice-Hall Inc., Englewood Cliffs, 1975)
40. M. Kotani, T. Sunada, *Trans. AMS* **353**, 1–20 (2000)
41. T. Sunada, *Jpn. J. Math.* **7**, 1–39 (2012)